

# Precise determination of the optical properties of turbid media using an optimized integrating sphere and advanced Monte Carlo simulations. Part 1: theory

FLORIAN FOSCHUM,\* FLORIAN BERGMANN,  AND ALWIN KIENLE

Institut für Lasertechnologien in der Medizin und Meßtechnik an der Universität Ulm, Helmholtzstr. 12, D-89081 Ulm, Germany

\*Corresponding author: [florian.foschum@ilm-ulm.de](mailto:florian.foschum@ilm-ulm.de)

Received 16 December 2019; revised 21 February 2020; accepted 25 February 2020; posted 26 February 2020 (Doc. ID 386011); published 30 March 2020

---

In this paper, we describe a method used to determine the optical properties, namely, the effective scattering and absorption coefficients, employing an optimized three-dimensional-printed single integrating sphere. The paper consists of two parts, and in Part 1, the theoretical investigation of an optimized measurement and the evaluation routine are presented. Using an analytical and a numerical model for the optical characterization of the integrating sphere, errors caused by the application of a non-ideal sphere (the one with ports or baffles) were investigated. Considering this research, a procedure for the precise determination of the optical properties, based on Monte Carlo simulations of the light distribution within the sample, was developed. In Part 2, we present the experimental validation of this procedure. © 2020 Optical Society of America

<https://doi.org/10.1364/AO.386011>

---

## 1. INTRODUCTION

The aim of this work is to develop a method to precisely determine the scattering and absorption properties of turbid media using an integrating sphere. In the literature, there are many works examining the optics of an integrating sphere in general, beginning with the work of Sumpner [1] and Ulbricht [2] more than 100 years ago. In contrast, although the number of papers dealing with determining of the optical properties, especially the effective scattering and absorption coefficients, using an integrating sphere is not excessive, still, quite a few papers can be found. In principle, the described methods determining the optical properties can be categorized into two groups. First is the use of a single integrating sphere with the need for changing the sample, the calibration standard, or the illumination geometry, to measure the total hemispherical reflectance and transmittance from a sample (see e.g., [3–6]). Second is the double integrating sphere setup with the need for corrections concerning the crosstalk between the two spheres (see e.g., [7–9]). The determination of the optical properties from integrating sphere measurements using Monte Carlo simulations in combination with look-up tables has been described in the literature [10–13].

In this study, a single-integrating-sphere setup was investigated. We note, however, that parts of the obtained results are also applicable to a double-integrating-sphere setup. We developed and implemented an analytical and a numerical

model (the latter was accelerated using GPUs) to study the light throughput of the used integrating sphere in order to minimize systematic errors. We ended up with a single-integrating-sphere setup without any baffle, as we showed that the baffle itself causes significant errors. We therefore, theoretically, have to consider the port losses, the direct illumination of the detector, and the disturbed sphere throughput due to the sample and calibration standards using the analytical model. To do so, a new two-stage evaluation process was developed. First, the illumination of all parts of the integrating sphere by the emitted light from the sample within the first strike was calculated by means of Monte Carlo simulations. In the second step, the effective detector signal was determined by an analytic model of the sphere throughput. In addition, the altered sphere throughput due to different situations at the ports and corrections of some minor assumptions within the model were considered using a normalization beam. Similar methods for correction of the altered sphere throughput have already been used [14]. Further, it has been shown that at least for the sample port, a knife edge is crucial. For the used port dimensions (diameter, 25 mm; height, 0.2 mm), Tang *et al.* [15] showed that the effects on the determination of the optical properties were only minor. Within this theoretical background, an optimized integrating sphere was designed, manufactured by a three-dimensional-printing technique and professionally coated. An extensive evaluation

was applied to the proposed setup, in which we were able to show a good performance of the introduced method, even for small absorption coefficients, with typical errors of the effective scattering coefficients and of the absorption coefficient being approximately 1% and 3%, respectively, in a large range of these values. The printed setup and the validation are described in Part 2 of this publication [16]. Moreover, the errors regarding the determined absorption and effective scattering caused by an inexact assumption of the thickness, the refractive index, and the scattering phase function of the sample were investigated.

In this paper, first, we introduce the setup. Subsequently, the numerical and the analytical models used for the calculation of the sphere throughput are presented and validated next to the GPU-accelerated Monte Carlo method for the calculation of the light distribution within the scattering sample. Based on the theoretical models, errors according the sphere throughput originating from a non-ideal sphere (e.g., having ports and baffles) are analyzed. Then, an optimized procedure to determine the optical properties is introduced, based on the theoretical investigations followed by the error analysis caused by inexact assumption of the sample properties.

## 2. SETUP

A main feature of an integrating sphere is the mixing of the radiant power from an angularly non-uniform radiating source, enabling an angularly independent measurement. For the determination of the optical properties of scattering samples, the radiant source is the overall radiant power reflected or transmitted from a turbid sample layer through the sample port into the sphere. The total hemispherical reflectance of the sample is thereby compounded by the surface reflectance and the volume reflectance. The surface reflectance again can be specular or diffuse, depending on the surface roughness. The main problem using a physical integrating sphere is that the ideal sphere geometry is disturbed by ports needed for interaction with the sphere. The problems with these ports are, on the one hand, that they can directly be illuminated from the radiant source (e.g., from the sample at another port) within the first strike, which leads to a loss of energy. On the other hand, they disturb the mixing process of the integrating sphere leading to a defective sphere throughput compared to the ideal theoretical one, especially for different materials (having different total hemispherical reflection coefficients  $\rho$ ) at the ports during the measurement procedure. Therefore, small port diameters and, thus, a small fraction of the port surface compared to the sphere surface, are often proposed to minimize the errors [17–19]. In addition, the detector or the detector field of view (FOV) of a non-Lambertian detector can, in principle, be directly illuminated by the radiant source, which contributes to the detector signal due to irradiation that has not undergone the mixing process within the sphere. We note that, if the detector has no Lambertian characteristics, the direct FOV illumination, which is the part of the sphere surface seen from the detector, is crucial. The comparison of radiant sources with different angular distributions leads to systematic differences when the mentioned effects are not taken into account. Concerning the direct irradiation of the detector from the radiant source,

different methods are conceivable for its consideration. In principle, a baffle can be used in the integrating sphere to avoid this direct radiation. However, we will show that even a baffle with minimized size disturbs the mixing process within the sphere in such a way that significant systematic errors occur. Thus, we propose to consider the irradiation on the detector by evaluating the optical properties and, additionally, calculating this contribution for scattering samples using the radiative transfer theory. For this purpose, a self-written, optimized, GPU-based Monte Carlo simulation was used. Also, for the used calibration standard, the angular distribution of the reflected light has to be determined and regarded in the evaluation of the optical properties (see second part of the paper [16]). Nevertheless, the consideration of the angular distribution of the sample and the calibration standard opposes the integrating sphere principle of a directional independent measurement. Therefore, without any baffle, a measurement of radiant sources having unknown angular distributions without the theoretical background is not feasible.

Concerning the change of the sphere throughput due to a change in reflectance coefficients within the ports by exchanging, for example, the sample with the calibration standard, different methods have been proposed. Within the substitution method, the sample is exchanged with the calibration standard at a single port of the sphere, and the altered sphere throughput is considered theoretically [20]. In the comparison method, two ports are used to attach the sample and the calibration standard to the sphere at the same time during sample and calibration measurement. However, within the comparison method a (further) baffle has to be used to avoid direct irradiation between the sample and the calibration standard [21]. Based on our investigations, we propose a modification of the substitution method using an additional normalization beam pointing onto the sphere wall to account for the altered sphere throughput due to different situations at the ports and for assumptions made in the analytical model used for correction of the sphere throughput, the port losses, and direct illumination of the detector. This method, additionally, has the advantage that the calibration measurement is independent of the sample measurement and, therefore, only has to be done once even for many samples.

With the introduced setup, we aim to determine the absorption coefficient  $\mu_a$  and the effective scattering coefficient  $\mu'_s$  of turbid media within a large range of  $1e-3 \text{ mm}^{-1} < \mu_a < 10 \text{ mm}^{-1}$  and  $0.2 \text{ mm}^{-1} < \mu'_s < 100 \text{ mm}^{-1}$ . Outside this range, systematic errors due to, for example, internal stray light in the spectrometer have a larger influence, as the dependence of the detected signal on the change of the optical properties reduces.

We do not propose measuring the collimated transmission simultaneously with the diffuse transmission [22], because to obtain a good signal for the collimated transmission, the optical thickness of the sample has to be small. Thus, the measurement of the diffuse transmission will become less precise, and the evaluation of the integrating sphere data depends more strongly on the exact form of the scattering phase function. We rather propose to use, additionally, a separate and optimized collimated transmittance setup to measure a second, optically thinner sample of the same material. Thus, the separately determined extinction coefficient can then be used for a more

precise determination of the effective scattering and absorption coefficients.

The whole measurement procedure is divided into two parts: the calibration and the sample measurements (compare Fig. 1). For the calibration procedure, first, the detector signals  $C_{RB}^R$  and  $C_{TB}^T$  are recorded. The calibration standards are, hereby, a physical standard for the total hemispherical reflectance measurement and simply the open port for the total hemispherical transmittance measurement. Here, the lower index labels the kind of the incident beam (subscript RB, reflection beam; subscript TB, transmission beam), whereas  $C^R$  indicates the calibration sample for the total hemispherical reflectance measurements and  $C^T$  the calibration standard for the transmittance measurements. In a second step, for both calibration standard configurations, the normalization measurement has to be performed resulting in the detector signals  $C_{NB}^R$  and  $C_{NB}^T$  with the subscript NB. For the sample measurement procedure, first, the sample  $S$  is successively illuminated by the reflection and the transmission beam, resulting in the detector signals  $S_{RB}$  and  $S_{TB}$ , respectively. As the sphere throughput changes with the altered reflectance coefficient at the sample port, again the normalization measurement has to be performed resulting in the detector signal  $S_{NB}$ . This measurement is the same for reflectance and transmittance measurements. Note that for real measurements, each signal has to be corrected by the corresponding dark measurement. The total hemispherical reflectance  $R$  and the transmittance  $T$  signals can then be calculated by

$$R = \frac{S_{RB} C_{NB}^R}{S_{NB} C_{RB}^R} \rho_{cal}; \quad T = \frac{S_{TB} C_{NB}^T}{S_{NB} C_{TB}^T}. \quad (1)$$

Thereby,  $\rho_{cal}$  is the reflectance coefficient of the used calibration standard at the corresponding wavelength. The setup used for this method, described in detail in the second part of the publication [16], consists, in principle, of an integrating sphere with a diameter of 150 mm. The sample is attached at a sample port of 25 mm in diameter having a knife edge to avoid reflections at the port edge. In addition, three further ports were used, one for the entry of the reflection beam, one for the entry of the normalization beam, and one for the detector, respectively. Three different light paths were applied, namely the reflection beam RB, the transmission beam TB, and the normalization beam NB. In Fig. 2, a sketch of the used setup is shown. The sample is illuminated under a  $5^\circ$  angle to the surface normal of the sample to measure the total hemispherical reflectance. We decided to measure the total hemispherical reflectance, including the surface reflectance, as with slightly rough surfaces, guiding the surface reflectance through a further port is error prone. For the transmittance measurement, also the  $5^\circ$  angle was used to simplify the evaluation as only one simulation is necessary for calculation of both signals and so that the transmission beam hits the sphere wall during the calibration measurement. For detection, an imaging technique was applied, i.e., two small adjoining parts of the sphere surface (6 mm in diameter) located near the south pole (compare Fig. 2, right) of the sphere were imaged to the distal end face of two optical fibers (1 mm in diameter). One fiber directs the detected light to a spectrometer for the visible spectral range, and the other fiber to spectrometer for the near-infrared spectral range, respectively. With this

technique, in contrast to a bare fiber pointing into the sphere with an unknown angular distribution, the FOV is defined and can easily be used in the simulations. Furthermore, if the coating of the sphere wall is Lambertian, which means that the reflected radiant power is proportional to the cosine of the angle between the surface normal and the scattered direction independent of the incident direction, we also get a Lambertian behavior of the detector.

### 3. THEORY

#### A. Numerical (Ray-tracing) Method for Calculation of the Integrating Sphere Throughput

A numerical simulation for the calculation of the sphere throughput was programmed similarly as described in the literature [23–25]. Additionally, we accelerated the simulation by a GPU implementation. Within this simulation, “photons” can be started from a radiant source at an arbitrary position within the sphere having an arbitrary angular distribution. The simulation traces each photon on its way through the sphere until it is absorbed by the sphere wall or transmitted through one of the ports. At each interaction with any surface of the sphere wall, the chance of absorption is regarded by means of the reflectance factor. To investigate the effects of the different ports of the sphere used for illumination, detection, or positioning of the sample, these ports can be included in the simulation having distinct positions within the sphere wall. The simulation includes both, ports representing spherical caps as well as flat ports. The reflection at the sphere wall, as well as that of the material within the ports can, in principle, have an arbitrary angular distribution. However, for the further investigations, only the two extreme cases, namely the pure specular and the Lambertian cosine distribution, were used. To analyze the effect of optional baffles, it is also possible to include elliptic surfaces at arbitrary positions with arbitrary orientations within the sphere. The baffle itself can exhibit a distinct reflectance coefficient and arbitrary angular distribution for the reflected light.

For validation of the numerical model, as well as for correction of the measured data, we further implemented an analytical model.

#### B. Analytical Model for the Throughput of the Integrating Sphere

The analytical model for the calculation of the sphere throughput was implemented following the ideas by Jacques *et al.* and Goebel and Finkel [20,26,27]. In the model, a Lambertian reflectance for all surfaces, ports that are part of the sphere wall (spherical caps), and the absence of any baffle are assumed. For this case, a simple model for the sphere throughput can be derived. First, it can be shown that the radiant power from a Lambertian source located at the sphere wall, which irradiates an arbitrarily located area at the sphere wall, can be calculated by multiplying the total emitted radiant power by the fraction of the irradiated area to the area of the whole inner surface of the sphere. Second, for the description of a sphere having ports, the sphere is divided into different areas  $A_n$ , namely, the inner sphere surface without the ports  $A_1$  and the area of the  $M$ th port  $A_{1+M}$  (compare Fig. 3). Further, we define the area of the

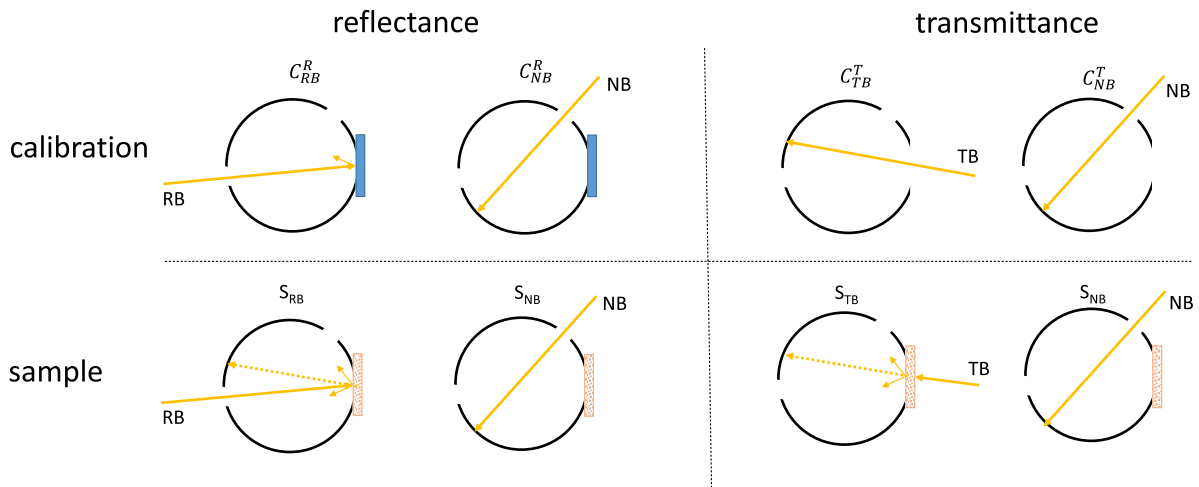


**Fig. 1.** Proposed configurations at the sphere for measurement of the single signals of the reference and the sample for the determination of the total hemispherical reflectance and transmittance.

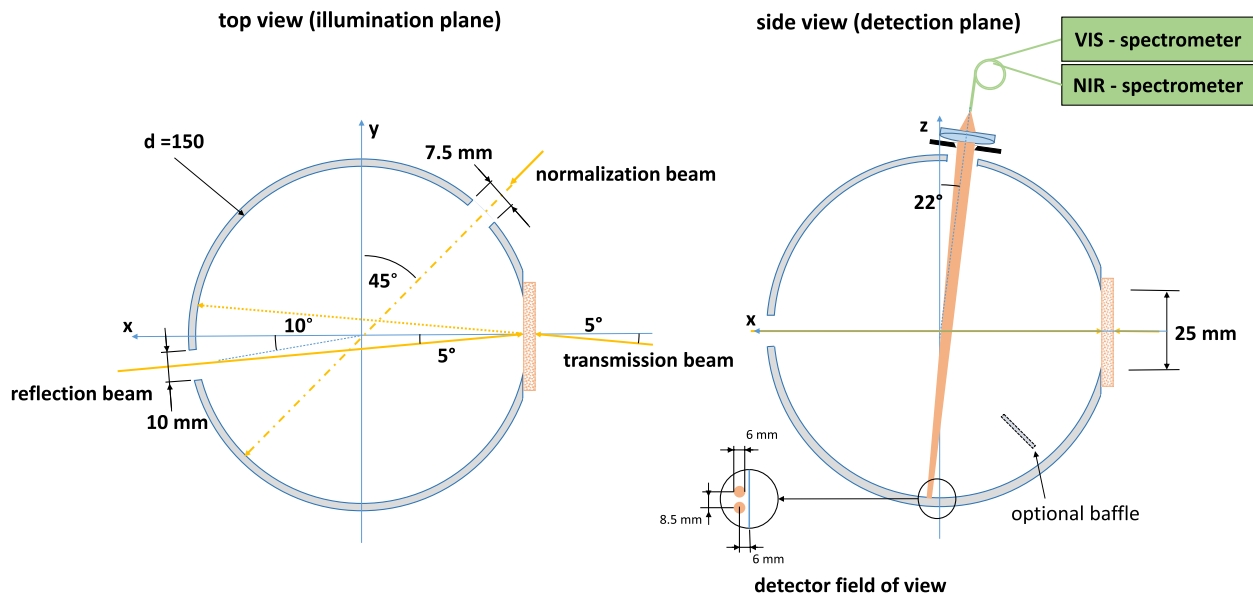


**Fig. 2.** Schematic of the used integrating sphere setup. Left, the sectional representation in the equatorial plane in the top view. Right, the vertical sectional representation in the front view.

detector  $A_D$ . The radiant power reaching the detector  $\Phi_D$  is composed of the direct illumination  $\Phi_{D0}$  and the irradiance from all surfaces of the sphere. Thereby, all interactions between the different surfaces have to be considered. These multiple interactions can be expressed in terms of a geometric series. In this context, within the model, the sensitivity of the detector is considered to be independent of the illumination direction. The input of the model is the radiant power  $\Phi_n$ , irradiating each surface  $A_n$  within the sphere and the direct illumination of the detector  $\Phi_{D0}$ . For a collimated source,  $\Phi_n$  is equal to the radiant power of the source  $\Phi_S$  for the surface  $n$ , which is illuminated by the beam and zero for all other surfaces. For Lambertian sources,  $\Phi_n$  can be calculated for each surface by the fraction of the area of the particular surface and the area of the whole inner sphere wall. For scattering samples,  $\Phi_n$  can be determined by means of

Monte Carlo simulations, considering the actual angular distribution. The total radiant power emitted from the source  $\Phi_S$  is thereby the sum over all  $\Phi_n$ , as  $\Phi_S$  is apportioned among the different surfaces. Note that the detector FOV is treated as a part of the sphere wall, and therefore,  $\Phi_1$  of the sphere wall includes  $\Phi_{D0}$  to incorporate this radiant power for the calculation of the multiple reflections. Therewith, the detection surface is not part of  $A_n$ . If the detector FOV is used, the actual radiant power on the detector has to be calculated by means of the Lambert law. Hereafter, the single terms of the infinite sum will be introduced. First, the radiant source can directly illuminate the detector with the radiant power  $\Phi_{D0}$  (see Fig. 3). The radiant power irradiating the detector after the first interaction with the single surfaces of the sphere can be expressed as

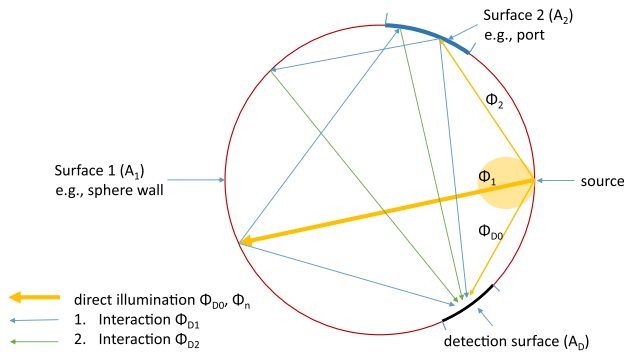


**Fig. 3.** Illustration of the different interactions between the different surfaces within the sphere and the detection surface.

$$\Phi_{D1} = \frac{A_{det}}{A_{sph}} \sum_{n=1}^N \rho_n \Phi_n, \quad (2)$$

whereby each surface  $A_n$ , which is irradiated from the source by the initial radiant power  $\Phi_n$  from the radiant source, emits the radiant power  $\rho_n \Phi_n$  according to their total hemispherical reflectance  $\rho_n$  and contributes to the detector power by the ratio  $A_{det}/A_{sph}$  of the detector surface  $A_{det}$  and the surface of the whole inner sphere surface  $A_{sph}$ , assuming a Lambertian characteristic. The radiant power radiating the detector after the second interaction can be calculated by

$$\Phi_{D2} = \frac{A_{det}}{A_{sph}} \sum_{l=1}^N \rho_l \frac{A_l}{A_{sph}} \sum_{n=1}^N \rho_n \Phi_n, \quad (3)$$

where first the irradiation of each surface  $A_l$  originating from the first interaction with all other surfaces (right sum) and afterwards the contribution to the detected power (left sum) is calculated. For each further interaction  $k$ , one has to sum over all contributions to each surface of the preceding interactions and then calculate the contribution to the irradiance of the detector. The  $k$ -th contribution can be expressed as

$$\Phi_{Dk} = \frac{A_{det}}{A_{sph}} \sum_{n=1}^N \rho_n \Phi_n \left( \sum_{l=1}^N \rho_l \frac{A_l}{A_{sph}} \right)^{k-1}. \quad (4)$$

Finally, the total radiant power at the detector applying a geometric series is

$$\begin{aligned} \Phi_D &= \Phi_{D0} + \sum_{k=1}^{\infty} \Phi_{Dk} \\ &= \Phi_{D0} + \frac{A_{det}}{A_{sph}} \sum_{n=1}^N \rho_n \Phi_n \left( 1 - \sum_{l=1}^N \rho_l \frac{A_l}{A_{sph}} \right)^{-1}. \end{aligned} \quad (5)$$

By using this formula, the radiant power at the detector FOV can be calculated for different source scenarios by adapting the initial radiant powers  $\Phi_{D0}$  and  $\Phi_n$ , the total hemispherical reflectance of each surface  $\rho_n$ , and the area of the whole surface  $A_n$ . If  $\rho_n = 0$ , the surface corresponds to an open port, as no radiant power is reflected.

### C. Cross Validation of the Numerical and the Analytical Theory

For the cross validation, the situation of the integrating sphere setup described in Section 2 (see Fig. 2) was used. To compare the analytical model and the ray tracer, all ports were set to be spherical caps having a Lambertian angular distribution, and no baffle was included. We used a sphere with a reflectance coefficient of  $\rho_{sph} = 0.98$ . The sphere had four ports with the positions and dimensions as shown in Fig. 2. The detector FOV was set to be a spherical cap with a diameter of 6 mm close to the south pole of the sphere. With both models, only the power irradiating the detector FOV was determined, and the actual detected signal was not calculated explicitly. However, as the conversation from the radiant power in the FOV and the radiant power of the detector is always the same constant factor, these values can directly be compared. To reenact the determination of the total hemispherical transmittance of a scattering sample, four different illumination scenarios were simulated with the numerical as well as with the analytical model. The reflectance coefficients of the open ports were set to zero as no light is reflected. All simulations were normalized to a total incident radiant power of  $\Phi_S = 1$  W. The surfaces were treated in the following order:  $n = 1$  was the surface of the sphere without any ports,  $n = 2$  the sample port, and  $n = 3$  to  $n = 5$  the three additional ports.

For Scenario 1, the calibration measurement for the transmission beam, and therewith the signal  $C_{TB}^T$  at the detector FOV, was simulated. As in this measurement the sample port remains open, the transmission beam was modeled to be a collimated beam pointing to the sphere wall next to the reflection beam entrance port. For the analytical model, this means that  $\Phi_{D0} = 0$ , as no light directly radiates the detector, and  $\Phi_1 = 1$  W, as the total power irradiates the sphere wall. The irradiation of the four ports was set to  $\Phi_{2-5} = 0$ , as they were not irradiated by the source. The reflectance coefficients of all ports  $\rho_{2-5}$  was set to 0, as all ports remain open. In Scenario 2, the calibration measurement using the normalization beam with the detector signal  $C_{NB}^T$  has been modeled. Therefore, the sphere configuration remains the same as in Scenario 1, and only the source changes to the normalization beam radiating collimated the sphere wall. As this simulation is in principle the same as the one in Scenario 1, the same results are expected for the numerical simulation. The analytical model is identical with the one in Scenario 1. In Scenario 3, the measured signal of a sample  $S_{TB}$  having a total hemispherical transmittance of  $T = 0.5$  and a cosine angular distribution was modeled. The reflectance coefficient of the sample port was set to  $\rho_2 = 0.5$ . As the sample radiates in a Lambertian manner, the direct illumination of the detector FOV and the ports have to be considered. Therefore, the irradiation of the detector is  $\Phi_{D0} = \Phi_S 0.5 A_{det}/A_{sph}$ , and the irradiation of all other surfaces  $\Phi_{1-5} = \Phi_S 0.5 A_{1-5}/A_{sph}$ . Scenario 4 models the normalization beam signal  $S_{NB}$  with an added sample at the port. The source is again pointing collimated to the sphere wall as modeled in Scenario 2, except that the sample port is covered with the sample ( $\rho_1 = 0.5$ ).

For the numerical solutions,  $1e9$  photons were launched three times, the results were averaged, and the relative standard deviation was calculated. In Table 1, the results for the four

**Table 1. Results of the Sphere Throughput for the Four Different Scenarios Obtained by the Numerical Model (num) and the Analytical Model (ana)**

	Scenario 1 ( $C_{TB}^T$ )	Scenario 2 ( $C_{NB}^T$ )	Scenario 3 ( $S_{TB}$ )	Scenario 4 ( $S_{NB}$ )
num	$1.0307\text{e-}2 \pm 0.95\text{e-}5$	$1.0303\text{e-}2 \pm 1.01\text{e-}5$	$0.5786\text{e-}2 \pm 5.1\text{e-}6$	$1.1350\text{e-}2 \pm 1.1\text{e-}5$
ana	$1.0303\text{e-}2$	$1.0303\text{e-}2$	$0.5789\text{e-}2$	$1.1346\text{e-}2$

scenarios calculated with both models are shown. Both methods agree within the statistical error of the numerical simulation, which was determined to be smaller than 0.1%. The results of Scenarios 1 and 2 are, as expected, the same, as for a sphere with Lambertian surface characteristics, the detector signal is independent of the impinging angle and position of the beam. The effect of the changing sphere throughput by altering from the open port to the port covered with the sample can clearly be observed by comparing Scenarios 2 and 4, where the same illumination was used. Note that the detected signal changes by about 10%.

To calculate the total reflected and transmitted power of a turbid sample, as well as the fraction of the power irradiating directly the ports and the detector, an efficient Monte Carlo solution of the radiative transfer theory was implemented.

#### D. Monte Carlo Solution of the Light Distribution in the Scattering Sample

For an efficient calculation of the light distribution in a scattering sample, a GPU-accelerated Monte Carlo simulation was implemented following the principles of Alerstam *et al.* [28,29]. Besides the functionality introduced by Alerstam, where a stack of lateral infinite layers was applied, radially and axially stacked cylindrically shaped simulation volumes were implemented to account for side losses of the sample and to include cylindrical cuvette holders. Furthermore, the detector for the integrating sphere measurements was extended. For reduction of the calculation time, a method was implemented to calculate the light distribution through the turbid medium for arbitrary absorption coefficients  $\mu_{a(\text{scaled})}$ , with a single Monte Carlo simulation [30,31]. In this method, the scalability relation of the absorption coefficient applying Beer's law and the path length  $l$  of each photon through the scattering medium was used. Each photon leaving the simulation volume is hereby weighted by

$$w = \exp^{-(\mu_{a(\text{scaled})} - \mu_{a(\text{sim})})l}, \quad (6)$$

where  $\mu_{a(\text{sim})}$  is the absorption coefficient of the original simulation. This method significantly reduces the calculation time for the used look-up tables. Note, if a multi-volume approach for the scattering medium is used, one has to distinguish between the different path lengths in the different volumes. This method was combined with the integrating sphere detector to calculate the total reflected and transmitted photons, by collecting all photons independent of the exiting direction within the diameter of the cylindrical port. All photons outside the ports were neglected.

To account for the irradiation within the first strike of the additional ports and the direct illumination of the detector

from the sample, the simulation was extended to calculate these values in combination with the scaled  $\mu_a$  method as follows. For each photon leaving the simulation volume through the sample port of the sphere either in reflectance or transmittance, the intersection with the other ports of the sphere and the detector is checked. If an intersection exists, the corresponding elements are incremented by the weights according to the scaled  $\mu_a$  method. These values are used together with the total reflected and transmitted photons within the sample port to calculate the actual detector signals using the analytic theory.

In general, the introduced code was tested extensively against different other Monte Carlo codes and analytical solutions of the radiative transfer equation (RTE). As an example, the total hemispherical reflectance and the transmittance of an infinitely extended slab (refractive index of  $n = 1.4$ ) using an infinitely large sample port were compared to other methods. Hereby the values were calculated with the MCGPUILM code, using the scaled  $\mu_a$  technique. The comparison was done using the CUDAMCML code from Alerstam *et al.* [28] and the adding-doubling method from Prahl [32]. The latter is, in principle, an exact solution of the RTE for this geometry. The results are shown in Fig. 4. For this comparison, the total hemispherical reflectance and transmittance of two slabs having a thickness of 0.1 mm and 4 mm, respectively, were calculated for different absorption coefficients. For the scattering parameters, a scattering coefficient of  $\mu'_s = 4 \text{ mm}^{-1}$  and an anisotropy factor of  $g = 0.75$  based on the Henyey–Greenstein phase function [33] were applied. Using these parameters, the optical thickness  $\tau = d\mu'_s$  of the samples was 0.1 and 4, respectively. An agreement within the statistics of the numerical methods could be found.

A further important finding of these simulations is the flattening of the signals for low absorption coefficients. Especially for the thin sample (0.1 mm), the signals show almost no change for absorption coefficients between  $\mu_a = 1 \text{ e-}4 \text{ mm}^{-1}$  and  $\mu_a = 1 \text{ e-}2 \text{ mm}^{-1}$ . This is reasonable as the average path length of the photons in this geometry is short compared to  $1/\mu_a$ , and therewith, the dependence of the total hemispherical reflectance and transmittance on the absorption is very small for these low absorption coefficients. This leads to the conclusion that it is almost impossible to determine absorption coefficients below  $1 \text{ e-}2 \text{ mm}^{-1}$  for such a thin sample with the used effective scattering coefficient. Even for the medium with an optical thickness of  $\tau = 4$ , the result shows that only with an optimized setup with low systematic errors, the determination of absorption coefficients below  $1 \text{ e-}3 \text{ mm}^{-1}$  is possible. Therefore, the throughput of the integrating sphere has to be considered precisely.

#### 4. ANALYSIS OF THE SPHERE ERRORS

In the following part, the resulting errors with and without the use of a baffle are studied for extreme cases of the sample's angular resolved transmittance or reflectance. The two cases are a collimated beam, such as a specular reflection by a perfect mirror, and the cosine distribution. Note that for scattering samples with mismatched boundary conditions, the angular distribution is expected to be between these extreme cases, as a part of the radiant power is reflected at the plain surface in a specular

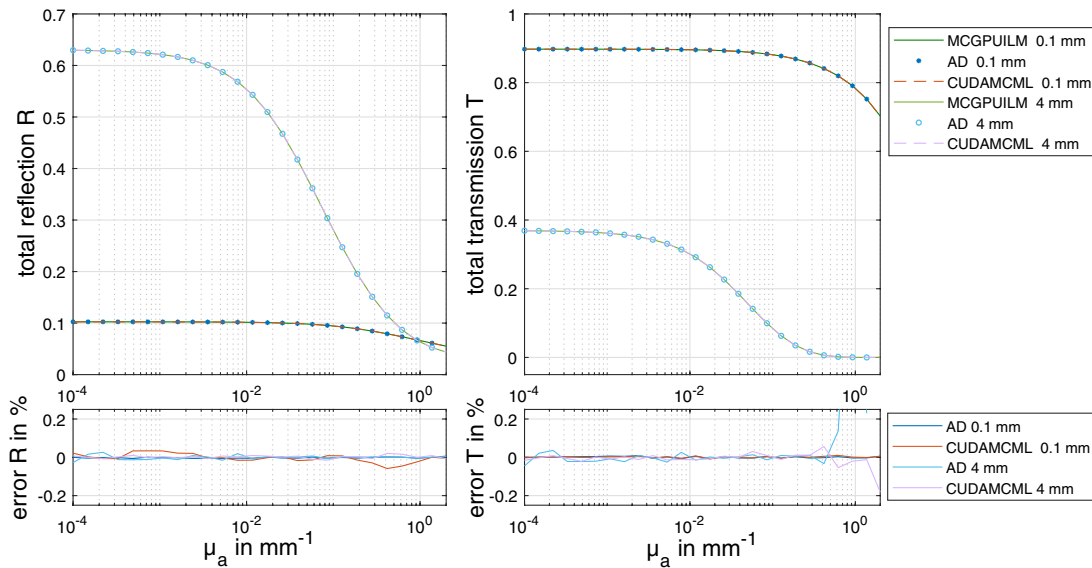


**Fig. 4.** Comparison of the total hemispherical reflectance and the transmittance of two lateral infinite slabs of 0.1 mm and 4 mm, respectively, versus the absorption coefficient. The comparison was made with the Monte Carlo code introduced in this paper using the scaled  $\mu_a$  technique MCGPUILM, the CUDAMCML code, and the adding-doubling method. In the lower plots, the relative error of the latter methods compared to the MCGPUILM code is shown.

**Table 2.** Results for the Numerical Model (num) and the Analytical Model (ana) When Both the Sample and the Calibration Standard Have a Lambertian Angular Distribution and No Baffle Is Applied<sup>a</sup>

	T	Error	t
num	0.4999 ± 0.0003	-0.02%	114 s
ana	0.5000	0%	0.003 s

<sup>a</sup>The total hemispherical transmittance T of the sample was set to  $T = 0.5$ .

manner, and the part scattered in the volume is reflected with an angular distribution similar to a Lambertian distribution [34].

**A. Investigations Without Baffle**

First, the errors obtained for a non-ideal sphere (with ports) without any baffle were investigated. Here, only an error is expected if the angularly resolved reflectance or transmittance from the sample and the calibration standards differs. To substantiate this prediction, first a sample and a calibration standard having both a Lambertian angular distribution were simulated (analytical and numerical) using the scenarios mentioned in the cross validation. The cosine distribution of the calibration standard is, thereby, just a hypothetical case. However, the general statement is transferable to the reflection case. For the numerical solution  $1e9$  photons were launched, and each simulation was calculated three times to estimate the statistical error. The resulting total hemispherical transmittance signal T for the sample was calculated according to Eq. (1), and the results are summarized in Table 2. As expected, for the same angular distribution of the transmitted light from the sample and calibration standard, the transmittance of  $T = 0.5$  is recovered correctly for both the analytical and the numerical models. The same result was found when both angular distributions were set

to be collimated. Consequently, if the angular distribution of the sample and the calibration standard is the same, there is no need for any correction. As this is usually not the case, the error was examined if a sample having a Lambertian angular transmittance was compared to a collimated calibration standard (as it is the case for the calibration of the transmittance measurement). This calculations were repeated for two different reflectance coefficients of the sphere wall of  $\rho_{sph} = 0.98$  and  $\rho_{sph} = 0.95$ . The results are shown in Table 3. If the angular distribution of the sample and the calibration standard differs, significant errors can be observed. The fact that the errors are in the range of  $1 - \rho_{sph}$  can be explained as follows. In case of the collimated illumination, the incident light first needs to be reflected at the sphere wall to reach a Lambertian angular distribution, as it is the case for the sample. However, during this first reflection, the radiant power is reduced by  $1 - \rho_{sph}$ . As the cosine source for the collimated case is at the sphere wall opposed to the sample port, it further has the ability to directly illuminate the sample surface, which is not the case for the Lambertian source at the sample. Therefore, the error is slightly larger than  $1 - \rho_{sph}$ , as the light has a higher ability to get absorbed at the sample.

For real samples, normally there is no calibration standard with identical angular distribution. Therefore, one approach is to use a baffle to shield the detector. As the baffle itself disturbs the light mixing within the sphere or, more precisely, interacts in a different way as the sphere wall with the ports, the errors using a baffle were investigated through the following simulations.

**B. Investigations Using a Baffle**

For the investigations including a baffle, only the numerical model could be used, as no baffle was included in the introduced analytical model. First, the influence of a baffle positioned exactly between the sample port and the detection FOV, having

**Table 3. Simulation Results of the Transmittance Signal of a Sample Having a Lambertian Angular Distribution Compared to a Calibration Standard Having a Specular Reflectance for a Sphere Without Baffle<sup>a</sup>**

	T	Error	t
num ( $\rho_{\text{sph}} = 0.98$ )	$0.5102 \pm 0.0001$	+2.04%	114 s
ana ( $\rho_{\text{sph}} = 0.98$ )	0.5102	+2.04%	0.003 s
num ( $\rho_{\text{sph}} = 0.95$ )	$0.5264 \pm 0.0001$	+5.28%	62 s
ana ( $\rho_{\text{sph}} = 0.95$ )	0.5263	+5.26%	0.003 s

<sup>a</sup>The total hemispherical transmittance T of the sample was set to  $T = 0.5$ . The reflectance coefficient of the sphere wall was set to  $\rho_{\text{sph}} = 0.98$ , as well as  $\rho_{\text{sph}} = 0.95$ .

**Table 4. Results for the Simulation When Both the Sample and Calibration Standards Have a Lambertian Angular Distribution and an Optimized Baffle Was Applied<sup>a</sup>**

	T	Error	t
num	$0.5019 \pm 0.0001$	+0.37%	114 s

<sup>a</sup>The total hemispherical transmittance T of the sample was set to  $T = 0.5$ .

an elliptical shape with the dimensions of 22.3 mm  $\times$  16.6 mm and the long axis pointing in the y direction (see Fig. 2), was investigated. The dimensions of the baffle were reduced so far that it was still not possible from any point within the sample port to illuminate the detection area. First, a simulation was carried out in which both, the sample and the calibration standard, had a Lambertian angular distribution. Note that without a baffle, no error was observed for this case. In Table 4, the results of this simulation are shown. In this simulation with identical angular resolved emission for the sample and the calibration standard, an error of about 0.37% occurs. This means that the baffle disturbs the sphere throughput, even for the same angular distribution of the sample and calibration standard. This results from the interaction of the reflected light from the baffle with the sample port that has a different reflectance coefficient for the sample and the calibration standard. As the baffle is closer to the sample port than the underlying part of the sphere, the probability of an interaction between the baffle and the port is higher. In this case, the port was open ( $\rho_p = 0$ ) for the calibration case and covered by the sample ( $\rho_p = 0.5$ ) during the sample case. As the irradiation of the port is higher via the baffle than by the sphere wall, more light is lost during the calibration measurement, and therefore, the signal from the sample is overrated.

Further, the error was investigated for a sample having a Lambertian angular resolved transmission and a calibration standard having a collimated angular reflectance. This analysis was done with an elliptical baffle of 22.3 mm  $\times$  16.6 mm, as well as with a larger circular baffle of 40 mm in diameter. The results are presented in Table 5. When using a baffle, indeed, the direct radiation of the detector is avoided, but as the baffle itself disturbs the sphere throughput, noticeable errors are also obtained. The error clearly depends on the size of the baffle. We note that we confirmed these errors experimentally (results not shown). If a baffle is, nevertheless, used, it's obvious to reduce

**Table 5. Results from the Simulation of a Sample with Lambertian Angular Distribution, Compared to a Specular Reflecting Calibration Standard Using Two Different Baffles<sup>a</sup>**

	T	Error	t
small baffle	$0.4918 \pm 0.0001$	-1.63%	142 s
large baffle	$0.4868 \pm 0.0001$	-2.62%	151 s

<sup>a</sup>The total hemispherical transmittance T of the sample was set to  $T = 0.5$ .

its size and use the mean distance between FOV and the sample port.

## 5. PROCEDURE FOR PRECISE DETERMINATION OF THE OPTICAL PROPERTIES

Even with the smallest usable baffle, errors of the sphere throughput of up to 1.6% occur and, therefore, it is not surprising that it is not possible to determine, for example, small absorption coefficients correctly with such a setup. Therefore, in principle, two methods are feasible to overcome this problem:

1. Measurements including a baffle and using a Monte Carlo simulation to calculate the light distribution in the scattering sample in combination with the numerical simulation of the integrating sphere including a baffle for the determination of the optical properties
2. Measurements without any baffle and using a Monte Carlo simulation to calculate the light distribution of the scattering sample in combination with the analytic model of the integrating sphere for the determination of the optical properties considering the direct illumination of the detector

For both cases, the actual angular distribution of the light from the sample (given by the Monte Carlo simulation) and the calibration standard (usually to be determined experimentally), as well as the wavelength-dependent reflectance coefficient of the sphere wall, have to be known. As the calculations needed for the first method are very time consuming, which is a problem when setting up the look-up table, the second method is preferred, although some minor assumptions are made in the application of the analytic model.

First, the angular distribution of the reflected light from the sphere wall coating, as well as of all materials within the ports, are assumed to be Lambertian, having only a single total hemispherical reflectance coefficient. Second, the ports are part of the sphere wall (spherical caps), which is not the case for the sample, for example. Third, the reflectance coefficient of the sample and the calibration standard has to be known if they are diffusely illuminated within the whole sample port from the integrating sphere. For the sample, this value was again calculated by means of the Monte Carlo simulation, by illumination of the sample with a Lambertian source with the diameter of the sample port. This is necessary as the total hemispherical reflection value using this illumination differs from the illumination using the reflection beam. Fourth, the detection port is assumed to be empty, but in the real setup, there is a lens that might reflect a small amount of light. Fifth, the reflectance coefficient of the

sphere wall is assumed to be constant over the whole sphere, although in our printed sphere, which is made out of two half spheres, there is an optical imperfection at the connection of the half spheres. Sixth, all ports are assumed to have a perfect knife edge shape. For the real ports, this is not the case, and therefore, reflections at the edges of the ports can occur.

Although for most of these points, the comparison with the corresponding numerical simulations shows (not shown here) that the effect on the determination of the optical properties is small, we decided to use a normalization beam to account for these errors. By using this normalization beam, the same errors in the mixing process within the sphere occur in the normalization measurement as in the sample measurement, and therefore, we can account for them. In addition, as the normalization beam, as well as the measurement beams, originates from the same halogen source, we can account for a long-term instability of the source. As for the calibration and the sample measurements, particular measurements with the normalization beam are made within a short period of time, long-term instabilities (between the calibration and the sample measurements) are canceled out [compare Eq. (1)].

Taking into account the investigations described above, we end up with the procedure shown in Fig. 5 for the determination of the optical properties. On the measurement side (Fig. 5, left, green), first the spectra of the different situations have to be acquired. This routine is divided into two independent parts: the calibration and the sample measurement procedure. We note that all spectra have to be subtracted by the corresponding dark spectrum. For the calibration of the reflection path, a reflective material has to be used. Commonly, a diffuse reflectance calibration standard is used for this purpose. These standards have the disadvantage that the reflectance coefficient has to be used as given by the manufacturer, if this quantity cannot be validated by an alternative measurement. These values do not consider any change of the reflectance coefficient of the calibration standard due to usage or aging. In addition, the angular distribution is not perfectly Lambertian, and it is not easy to determine the exact angular distribution accurately enough using, for example, a goniometric setup. However, the angular distribution is especially important for the calculation of the direct illumination of the detector. In addition, comparing the values given by the manufacturer for different standards of the same or different nominal reflectance, coefficients with our experimental setup led to a typical error of more than 1%. With this background, and additionally, having in mind the potential of the analytic correction of the sphere throughput for arbitrary angular distributions, we propose to use a mirror as a calibration standard. Using a mirror results in a well-defined angular distribution of the reflected light, and it is easy to determine the total hemispherical reflectance of the standard for collimated illumination. The method used for this purpose is explained in Part 2 of this publication [16]. For the calibration measurement in the transmittance case, we simply use the open port. Additionally, for both calibration configurations, the detector signal using the normalization beam has to be recorded. For the sample measurement, the sample simply has to be mounted at the sample port and is sequentially illuminated by the transmission, the reflection, and the normalization beam, while the detector signal is recorded for each case. In a second step, the

detector signal for the total hemispherical transmittance  $T$  and reflectance  $R$  from the sample have to be calculated [see Eq. (1)].

For the evaluation (Fig. 5, right, red), a look-up table for different effective scattering coefficients and absorption coefficients was calculated. For this, the GPU-accelerated Monte Carlo simulation records for different combinations of the optical coefficients the amount of total reflected and transmitted photons of the sample within the sample port, the irradiation on the additional ports, and the direct irradiation of the detector FOV. Subsequently, the reflectance coefficient of each combination of optical properties is calculated with the Monte Carlo simulation for a Lambertian irradiation within the diameter of the sample port, needed in the analytic model for the indirect illumination of the sample from the sphere within the mixing process.

For calculation of the LUT, the expected range of the optical parameters has to be defined and subdivided by an appropriate step size. Further, the refractive index of the sample  $n_{\text{medium}}$ , the refractive index of an optional cuvette  $n_{\text{glass}}$ , the thickness of the sample  $d$ , and eventually the asymmetry factor of the scattering phase function  $g$  have to be regarded for each distinct sample at each wavelength. To do so, different LUTs for these parameters have to be calculated and interpolated for the actual values. To find the optimal step size for each of the values, different LUTs have been calculated, and the interpolation was checked with additional calculations using values in between. For interpolation errors below 1%, we end up with the following discretization (see Table 6). For a single-layer sample therewith, using the scaling relation of the absorption coefficient 150,280 simulations, and for the sample covered by the cuvette, 450,840 simulations were calculated. Both cases were simulated using  $1e7$  photons. For storage, one set of  $\mu_a$  and  $\mu'_s$  values build one LUT. Each of these LUTs were stored in a LUT tree built by the other parameters. As total hemispherical transmittance signals  $T < 0.1\%$  can only be measured with large relative errors, the simulation results of total hemispherical transmittance signals below these values were discarded. In the evaluation procedure, the user is warned when the total hemispherical transmittance signal  $T_{is} < 0.1\%$ , and it is advised to use a thinner sample. Based on the calculated amount of reflected and transmitted photons onto the different surfaces of the sphere, the actual sphere throughput, and therefore, the expected detector signal (total hemispherical reflectance and transmittance signal) have to be calculated using the analytical model. Therefore, the averaged reflectance coefficient of the sphere wall is needed for the corresponding wavelength. For the evaluation of a distinct sample at a distinct wavelength, first, the LUTs of the adjacent values of  $n_{\text{medium}}$ ,  $d$ ,  $g$ , and ( $n_{\text{glass}}$ ) were found in the LUT tree. Then, the  $\mu'_s$  and  $\mu_a$  values were calculated from all of these LUTs considering the actual reflectance coefficient of the sphere wall. In the last step, the final  $\mu'_s$  and  $\mu_a$  values were calculated by linear interpolation. This was done using a recursive algorithm. For the determination of the optical properties from the single LUTs, we followed the ideas of Simpson *et al.* [3] by using an inverted LUT. Here, in principle, the LUT  $(\mu'_s, \mu_a) = \{R, T\}$ , which for distinct optical properties contains the corrected total hemispherical reflectance and transmittance signals, is inverted in a way that with LUT  $(R, T) = \mu'_s$  and LUT  $(R, T) = \mu_a$ , two independent look-up tables for both optical properties arise.

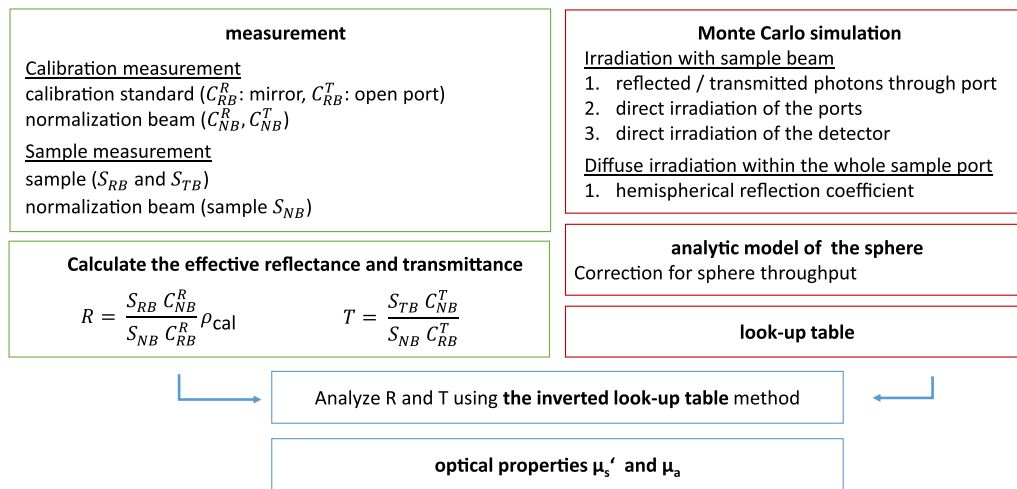


**Fig. 5.** Flow chart of the proposed procedure for precise determination of the optical properties.

**Table 6.** Discretization of the Single Values for Calculation of the Look-Up Table

Parameter	Range	Discretization	Count
$\mu_a$	1e-4 mm <sup>-1</sup> – 10 mm <sup>-1</sup>	56 logarithmic steps	56
$\mu_s'$	0.1 mm <sup>-1</sup> – 100 mm <sup>-1</sup>	34 logarithmic steps	34
$n_{\text{medium}}$	1 and 1.3–1.7	step size 0.025	17
$d$	0.1 mm–6.5 mm	step size 0.1 mm	56
$g$	0.5–0.99	0.5, 0.75, 0.9, 0.99	4
$n_{\text{glass}}$	1.49–1.56	step size 0.035	3

For the two-dimensional interpolation of the scattered data, a natural neighbor algorithm [35,36] based on the Delaunay triangulation [37] of the  $R$  and  $T$  values was used to determine the effective scattering and the absorption coefficients.

## 6. ERROR ANALYSIS

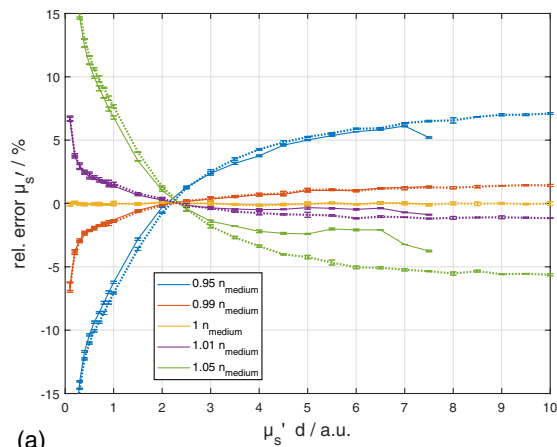
For turbid media, the refractive index  $n$  and the scattering phase function, frequently represented by the anisotropy factor  $g$ , are often not exactly known. Furthermore, the determination of the sample thickness can be prone to errors. These parameters have an impact on the solution of the inverse problem and, therefore, on the evaluated properties  $\mu_s'$  and  $\mu_a$ . Below, the influence of an inexact assumption of  $d$ ,  $n$ , and  $g$  on the determination of  $\mu_s'$  and  $\mu_a$  is reviewed using both an ideal (liquid) sample surrounded by a cuvette of  $d_{\text{glass}} = 1$  mm and  $n_{\text{glass}} = 1.5$ , and an ideal (solid) single-layer sample. The ideal sample is thereby defined as a homogeneous medium with perfect plane parallel surfaces. The optical properties were chosen to be  $n_{\text{medium}} = 1.33$ ,  $g = 0.75$ ,  $\mu_s' = 1$  mm<sup>-1</sup>,  $\mu_a = 0.1$  mm<sup>-1</sup> (solid line in Figs. 6 and 7), and  $\mu_a = 0.01$  mm<sup>-1</sup> (dotted line in Figs. 6 and 7). For the forward calculations, we used Monte Carlo simulations with  $1e7$  photons and modified  $d$ ,  $n$  (modification of  $-5\%$ ,  $-1\%$ ,  $1\%$ , and  $5\%$ ), or the  $g$  factor (modification values  $g$  of 0.5, 0.9, and 0.99). The resulting reflectance and transmittance values using the modified optical parameters were then fitted using a LUT of the ideal samples.

The whole analysis was repeated using different optical thicknesses  $\tau = \mu_s' d$  ranging from  $\tau = 0.1$  to 10 by changing the thickness  $d$  of the sample. We used three repetitions of each forward calculation to estimate the influence of the statistical errors of the Monte Carlo simulation. For the LUT of the ideal sample, we again used simulations using  $1e7$  photons with an increment in  $\mu_s'$  of  $0.05$  mm<sup>-1</sup> ranging from  $0.7$  mm<sup>-1</sup> to  $1.3$  mm<sup>-1</sup>, and with logarithmically scaled  $\mu_a$  values ranging from  $1e-4$  mm<sup>-1</sup> to  $1$  mm<sup>-1</sup> in 34 steps.

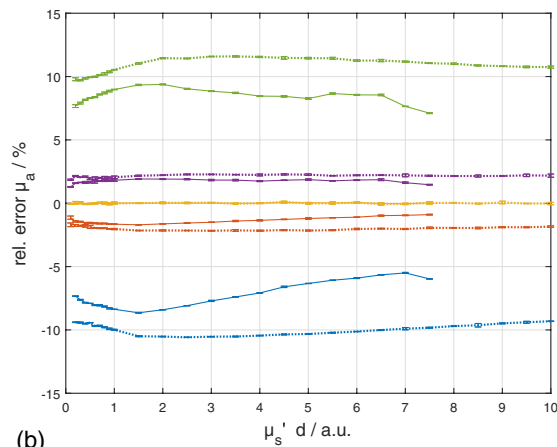
First, an incorrectly assumed thickness (not shown here) was investigated, leading to directly proportional changes in  $\mu_s'$  and  $\mu_a$ , which are independent and of  $\tau$ . This means for an actual thickness that was 1% higher than the thickness assumed for the evaluations, both  $\mu_s'$  and  $\mu_a$  are enhanced for around 1% compared to the real values.

Second, we analyzed the errors that occur for a wrong estimated refractive index  $n$ . The errors in  $\mu_s'$  for solid phantoms [see Fig. 6 (left)] and samples within a cuvette [see Fig. 7 (left)] for  $\tau > 1$  are similar. Below this optical thickness, the behavior differs, as for the relative low-scattering reflection at the interfaces becomes more important. The largest errors can be found for  $\tau < 1$  in case of solid phantoms reaching 15% relative error for a deviation of 5% of  $n_{\text{medium}}$ . The obtained relative errors for the different  $\mu_a$  values of  $0.1$  and  $0.01$  mm<sup>-1</sup> show similar behavior. However, for  $\mu_a = 0.1$  mm<sup>-1</sup> and  $\tau > 8$  the transmitted signal was below 0.1% and, therefore, the obtained errors are not shown. In the case of solid phantoms, a wrong estimated  $n_{\text{medium}}$  of +5% will change  $\mu_s'$  about +6% and  $\mu_a$  about +10% for the optimal sample thickness of  $\tau > 2$ . The errors for  $\mu_a$  are larger than for  $\mu_s'$  and in case of solid phantoms nearly independent of  $\tau$  [see Fig. 6 (right)]. For the samples within a cuvette, it shows that for higher  $\mu_a$ , larger relative errors of the determined  $\mu_a$  occur [see Fig. 7 (right)]. For the low  $\mu_a$ , the errors are similar to the ones of the single layer and are around 10% for a change of 5% for  $n$ . For the high  $\mu_a$ , errors up to 20% occur for the same situation.

Third, the simulations show that an incorrectly assumed asymmetry factor has a smaller influence on the determination of the optical properties than a wrong sample thickness or

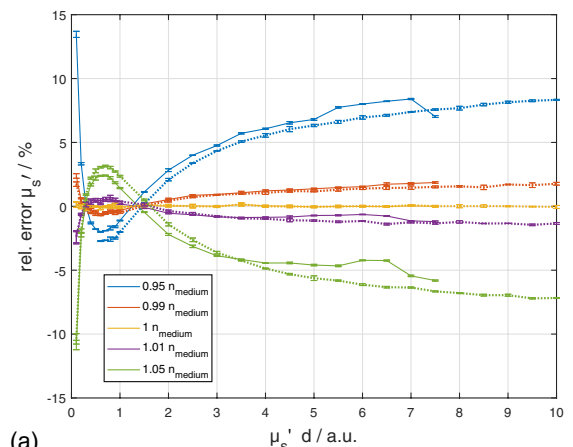


(a)

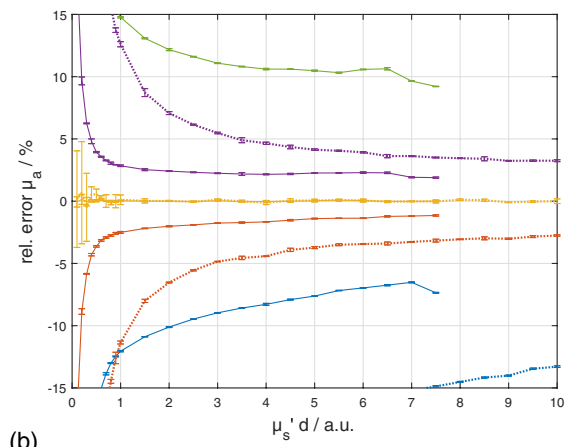


(b)

**Fig. 6.** Relative errors in  $\mu'_s$  (a) and  $\mu_a$  (b) due to a change in  $n$  versus  $\mu'_s d$  for a single layer phantom with a plane-parallel surface. Solid lines are used for  $\mu_a = 0.1 \text{ mm}^{-1}$  and the dotted lines for  $\mu_a = 0.01 \text{ mm}^{-1}$ .



(a)



(b)

**Fig. 7.** Relative errors in  $\mu'_s$  (a) and  $\mu_a$  (b) due to a change in  $n$  versus  $\mu'_s d$  for a sample within a cuvette. Solid lines are used for  $\mu_a = 0.1 \text{ mm}^{-1}$  and the dotted lines for  $\mu_a = 0.01 \text{ mm}^{-1}$ .

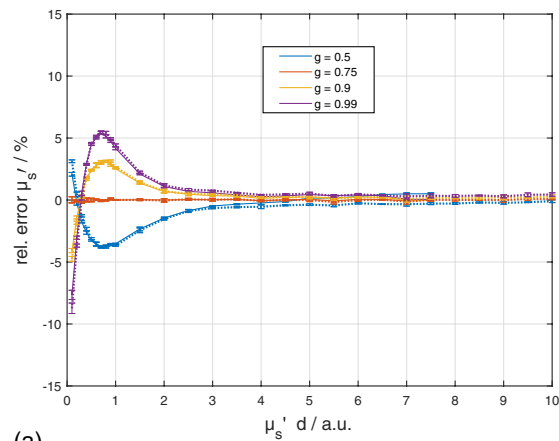
refractive index for  $\tau > 2$  (see Fig. 8). The relative deviation for  $\tau > 2$  and an assumed  $g = 0.5$  or  $g = 0.9$  instead of  $g = 0.75$  is typically below 1% for  $\mu'_s$  and below 2% for  $\mu_a$ . If the optical thickness gets smaller, the fraction of unscattered light, whose amount is directly linked to the asymmetry factor (for constant effective scattering) increases, compared to multiple scattered light. If this is not regarded by the scattering phase function, it will cause bigger uncertainties for a wrongly assumed  $g$ . In addition, for thin samples, the unscattered light can again be reflected at the samples backside and therefore change the light distribution within the sample. Hence, for thin samples, the influence of  $g$  on the light distribution is higher, which leads to higher errors in the optical properties if a wrong  $g$  is assumed.

Fourth, the errors caused by evaluating a sample with an actual scattering phase function described, e.g., by the Mie theory by means of the Henyey–Greenstein phase function were investigated. Therefore, forward calculations based on the phase function of polystyrene spheres having a diameter of  $2.74 \mu\text{m} \pm 0.05 \mu\text{m}$  at 600 nm were used. The scattering phase function was thereby calculated using the Mie theory [38]. The calculated reflectance and transmittance values were evaluated by means of the LUT based on the Henyey–Greenstein scattering phase function. For the LUT, two different asymmetry factors were used. First, the same asymmetry factor as for the

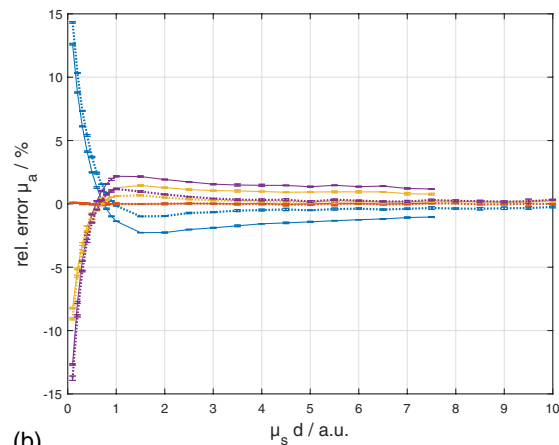
Mie scattering phase function ( $g = 0.82$ ) and, second,  $g = 0.75$  as used for a standard evaluation without knowledge of the scattering phase function were applied. The relative errors due to these assumptions regarding the scattering phase function for the effective scattering and the absorption coefficients were less than 1% for  $\tau > 2$ , almost independent of the used asymmetry factor (see Fig. 9). A larger absolute  $\mu_a$  results in slightly larger relative deviations in  $\mu_a$  comparing both investigated  $\mu_a = 0.1$  and  $0.01 \text{ mm}^{-1}$ . From this analysis, we conclude that an accurate determination of  $n$  and  $d$  is a key point in determining precise optical properties. A wrongly estimated asymmetry factor on the other side does not have a major influence, if a sufficient optical thickness of the sample,  $\tau > 2$ , is used.

## 7. CONCLUSION

In this work, we first provide an overview of the proposed optimized setup. A detailed description of this setup can be found in the second part of this two-part publication. Further a numerical model, based on a ray-tracing algorithm, is described for studying the sphere throughput of complex sphere geometries, including baffles. For efficient calculation of the sphere throughput of simpler sphere geometries, a numerical model was implemented following the ideas by Jacques *et al.* and



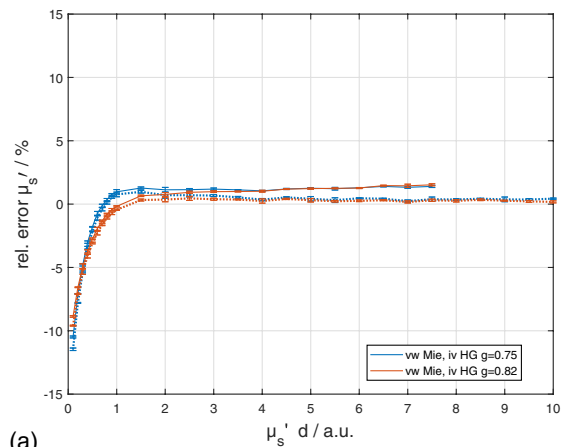
(a)



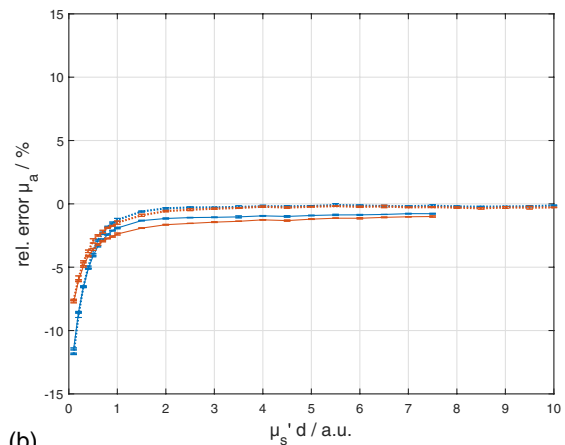
(b)

**Fig. 8.** Relative deviations in  $\mu'_s$  (a) and  $\mu_a$  (b) for a wrongly assumed asymmetry factor  $g$ . The evaluation is based on the Henyey–Greenstein scattering phase function. Solid lines are used for  $\mu_a = 0.1 \text{ mm}^{-1}$ , and the dotted lines for  $\mu_a = 0.01 \text{ mm}^{-1}$ .

Goebel and Finkel [20,26,27]. The cross validation between the numerical and the analytical models showed an exact agreement within the statistical errors of the numerical simulation. Using these models, the effects of energy loss through the ports of the sphere and the direct radiation of the FOV of the detector were shown. Further, the errors caused by a baffle for shielding the detector FOV from direct radiation were investigated, leading even for similar dependence of the angular resolved transmittance and reflectance of the sample and calibration standard to non-acceptable errors due to the disturbance of the light distribution within the sphere by the baffle. Therefore, an integrating sphere without any baffle was used. To correct for the direct illumination of the detector FOV and the ports, these values had to be calculated by the Monte Carlo simulation and considered during the evaluation of the samples. The optimized procedure for the precise determination of the optical properties, therefore, combines the results of the Monte Carlo simulation and the use of an analytic model of the sphere throughput to determine the optical properties correctly. We note that, by omitting the baffle, for precise measurements, the angular distribution of the light emitted by the sample has to be known, leading to erroneous measurements for samples with unknown angular distribution. The potential of the introduced method is shown in the second



(a)



(b)

**Fig. 9.** Relative deviations in  $\mu'_s$  (a) and  $\mu_a$  (b), if a Mie scattering phase function of polystyrene spheres is used for the forward calculation and the optical properties are evaluated by means of a Henyey–Greenstein scattering phase function using two different asymmetry factors. Solid lines are used for  $\mu_a = 0.1 \text{ mm}^{-1}$ , and the dotted lines for  $\mu_a = 0.01 \text{ mm}^{-1}$ .

part of this publication, in which we show through experiments that a broad range of optical properties can be determined precisely within the given measurement range with typically errors beyond a few percent. In addition, we show that the accuracy of the additional information regarding the thickness and the refractive index of the sample on the determination of the optical properties is a crucial point. On the other hand, we demonstrated that assumptions regarding the scattering phase function have only minor effects on the determination of the optical properties if the optical thickness of the sample is large enough ( $\tau > 2$ ).

In further work, the measurement range could be extended by reduction of the systematic errors caused by the minor assumptions listed in Section 5. For example, the non-Lambertian behavior of the sphere wall, which has no single hemispherical reflectance factor independent of the incident angle, and the non-empty ports having no ideal knife edges could be regarded in the evaluation process. Further, the setup could be extended for absolute measurements of the quantum efficiency of fluorescent media or the absolute determination of the Raman scattering cross section. Therefore, both effects have to be

included in the Monte Carlo simulation, and the LUT has to be adjusted accordingly. In addition, by measuring the reflectance and transmittance of different layers of the same material, which have different thicknesses, more information on the optical properties can be obtained. For example, the refractive index or parameters characterizing the scattering function can be determined. The information might be also obtained by using different illumination angles incident on the same sample.

**Funding.** Deutsche Forschungs Gemeinschaft; Bundesministerium für Wirtschaft und Energie

**Disclosures.** The authors declare that there are no conflicts of interest related to this paper.

## REFERENCES

- W. Sumpner, "The diffusion of light," *Proc. Phys. Soc. London* **12**, 10–29 (1893).
- R. Ulbricht, *Die Bestimmung der mittleren räumlichen Lichtintensität durch nur eine Messung* (1900).
- C. R. Simpson, M. Kohl, M. Essenpreis, and M. Cope, "Near-infrared optical properties of ex vivo human skin and subcutaneous tissues measured using the Monte Carlo inversion technique," *Phys. Med. Biol.* **43**, 2465–2478 (1998).
- A. Bashkatov, E. Genina, V. Kochubey, and V. Tuchin, "Optical properties of human skin, subcutaneous and mucous tissues in the wavelength range from 400 to 2000 nm," *J. Phys. D* **38**, 2543 (2005).
- M. Friebel, A. Roggan, G. J. Müller, and M. C. Meinke, "Determination of optical properties of human blood in the spectral range 250 to 1100 nm using Monte Carlo simulations with hematocrit-dependent effective scattering phase functions," *J. Biomed. Opt.* **11**, 034021 (2006).
- E. V. Salomatina, B. Jiang, J. Novak, and A. N. Yaroslavsky, "Optical properties of normal and cancerous human skin in the visible and near-infrared spectral range," *J. Biomed. Opt.* **11**, 064026 (2006).
- A. Roggan, "Measurements of optical tissue properties using integrating sphere technique," *Proc. SPIE* **10311**, 103110A (1993).
- J. W. Pickering, S. A. Prahl, N. Van Wieringen, J. F. Beek, H. J. Sterenborg, and M. J. Van Gemert, "Double-integrating-sphere system for measuring the optical properties of tissue," *Appl. Opt.* **32**, 399–410 (1993).
- J. Beek, P. Blokland, P. Posthumus, M. Aalders, J. Pickering, H. Sterenborg, and M. Van Gemert, "In vitro double-integrating-sphere optical properties of tissues between 630 and 1064 nm," *Phys. Med. Biol.* **42**, 2255–2261 (1997).
- N. B. Nelson and B. B. Prézelin, "Calibration of an integrating sphere for determining the absorption coefficient of scattering suspensions," *Appl. Opt.* **32**, 6710–6717 (1993).
- M. Hammer, A. Roggan, D. Schweitzer, and G. Müller, "Optical properties of ocular fundus tissues—an in vitro study using the double-integrating-sphere technique and inverse Monte Carlo simulation," *Phys. Med. Biol.* **40**, 963 (1995).
- A. M. Nilsson, R. Berg, and S. Andersson-Engels, "Measurements of the optical properties of tissue in conjunction with photodynamic therapy," *Appl. Opt.* **34**, 4609–4619 (1995).
- A. Roggan, M. Friebel, K. Dörschel, A. Hahn, and G. J. Müller, "Optical properties of circulating human blood in the wavelength range 400–2500 nm," *J. Biomed. Opt.* **4**, 36–47 (1999).
- P. Lemaillet, C. C. Cooksey, J. Hwang, H. Wabnitz, D. Grosenick, L. Yang, and D. W. Allen, "Correction of an adding-doubling inversion algorithm for the measurement of the optical parameters of turbid media," *Biomed. Opt. Express* **9**, 55–71 (2018).
- C. Tang, M. Meyer, B. L. Darby, B. Auguie, and E. C. Le Ru, "Realistic ports in integrating spheres: reflectance, transmittance, and angular redirection," *Appl. Opt.* **57**, 1581–1588 (2018).
- F. Bergmann, F. Foschum, and A. Kienle, "Precise determination of the optical properties of turbid media using an optimized integrating sphere and advanced monte carlo simulations. Part 2: experiments," *Appl. Opt.* **59**, 3216–3226 (2020).
- K. A. Snail and L. M. Hanssen, "Integrating sphere designs with isotropic throughput," *Appl. Opt.* **28**, 1793–1799 (1989).
- H. L. Tardy, "Matrix method for integrating-sphere calculations," *J. Opt. Soc. Am. A* **8**, 1411–1418 (1991).
- K. Carr, "Integrating sphere theory and applications. Part I: integrating sphere theory and design," *Surf. Coat. Int.* **80**, 380–385 (1997).
- J. A. Jacques and H. F. Kuppenheim, "Theory of the integrating sphere," *J. Opt. Soc. Am. A* **45**, 460–470 (1955).
- L. M. Hanssen and K. A. Snail, "Integrating spheres for mid-and near-infrared reflection spectroscopy," in *Handbook of Vibrational Spectroscopy* (2002), Vol. **2**, pp. 1175–1192.
- A. Roggan, O. Minet, C. Schroeder, and G. J. Mueller, "Determination of optical tissue properties with double integrating sphere technique and Monte Carlo simulations," *Proc. SPIE* **2100**, 42–56 (1994).
- B. G. Crowther, "Computer modeling of integrating spheres," *Appl. Opt.* **35**, 5880–5886 (1996).
- Y. Ohno and R. O. Daubach, "Integrating sphere simulation on spatial non-uniformity errors in luminous flux measurement," *J. Illum. Eng. Soc.* **30**, 105–115 (2001).
- A. V. Prokhorov, S. N. Mekhontsev, and L. M. Hanssen, "Monte Carlo modeling of an integrating sphere reflectometer," *Appl. Opt.* **42**, 3832–3842 (2003).
- D. G. Goebel, "Generalized integrating-sphere theory," *Appl. Opt.* **6**, 125–128 (1967).
- M. W. Finkel, "Integrating sphere theory," *Opt. Commun.* **2**, 25–28 (1970).
- E. Alerstam, T. Svensson, and S. Andersson-Engels, *User Manual and Implementation Notes* (2009).
- E. Alerstam, W. C. Y. Lo, T. D. Han, J. Rose, S. Andersson-Engels, and L. Lilje, "Next-generation acceleration and code optimization for light transport in turbid media using GPUs," *Biomed. Opt. Express* **1**, 658–675 (2010).
- A. Kienle and M. S. Patterson, "Determination of the optical properties of turbid media from a single Monte Carlo simulation," *Phys. Med. Biol.* **41**, 2221 (1996).
- E. Alerstam, S. Andersson-Engels, and T. Svensson, "White Monte Carlo for time-resolved photon migration," *J. Biomed. Opt.* **13**, 041304 (2008).
- S. A. Prahl, M. J. van Gemert, and A. J. Welch, "Determining the optical properties of turbid media by using the adding-doubling method," *Appl. Opt.* **32**, 559–568 (1993).
- L. G. Henyey and J. L. Greenstein, "Diffuse radiation in the galaxy," *Astrophys. J.* **93**, 70–83 (1941).
- A. Kienle and F. Foschum, "250 years lambert surface: does it really exist?" *Opt. Express* **19**, 3881–3889 (2011).
- R. Sibson, "A brief description of natural neighbour interpolation," in *Interpreting Multivariate Data* (1981).
- L. Liang and D. Hale, "A stable and fast implementation of natural neighbor interpolation," Technical Report CWP-657 (Center for Wave Phenomena, Colorado School of Mines, 2010).
- B. Delaunay, "Sur la sphere vide," *Izv. Akad. Nauk SSSR Otd. Biol. Nauk* **7**, 793–800 (1934).
- G. Mie, "Beiträge zur Optik trüber Medien, speziell kolloidaler Metallösungen," *Ann. Phys.* **330**, 377–445 (1908).